A SMART BI-DIRECTIONAL MODEL OF HEAT TRANSFER AND FREE SURFACE FLOW IN GAS-METAL-ARC FILLET WELDING FOR PRACTISING ENGINEERS

A. Kumar, W. Zhang, C.H. Kim, T. DebRoy
Department of Materials Science and Engineering, The Pennsylvania State University
(United States)
e-mail: debroy@psu.edu

ABSTRACT

In recent years, numerical heat transfer and fluid flow models have provided significant insight about fusion welding processes and welded materials. A major problem in their practical use is that several input parameters cannot be easily prescribed from fundamental principles. Available inverse models of fusion welding for the determination of these unknown parameters have ignored important physical processes such as convection in the weld pool to make computational tasks tractable. As a result, these models are not very different from the neural network type models that are not required to obey any physical law. A smart, bi-directional, numerical model has been developed to determine three-dimensional temperature and velocity profiles, weld geometry and the shape of the solidified weld reinforcement surface during gas metal arc (GMA) welding of fillet joints. Apart from the transport of heat from the welding arc, additional heat from the metal droplets was also considered in the model. The model is capable of estimating unknown parameters such as the arc efficiency, effective thermal conductivity and effective viscosity from a limited number of data on weld geometry based on multivariable optimisation. Alternative strategies for the optimisation are examined. The calculated shape and size of the fusion zone, finger penetration characteristic of the GMA welds and the solidified free surface profile were in fair agreement with the experimental results for various welding conditions. In particular, the computed values of the leg length, the penetration depth and the actual throat agreed well with those measured experimentally for various heat inputs. The weld thermal cycles and the cooling rates were also in good agreement with the independent experimental data. The research presented here shows that advances in computational hardware and software have now made construction of smart, bi-directional, large transport phenomena based phenomenological models a useful undertaking.

IIW-Thesaurus keywords: Arc welding; Gas shielded arc welding; GMA welding; Fillet welds; Mathematical models; Computation; Optimisation; Heat flow; Viscosity; Physical properties; Thermal conductivity; Thermal properties; Thermal cycling; Process conditions; Leg length; Dimensions; Size; Statistical methods; Reference lists.

1 INTRODUCTION

In the previous two decades, application of transport phenomena has resulted in improved understanding of complex fusion welding processes and welded materials. For example, numerical calculations of heat transfer and fluid flow in welding have enabled accurate quantitative calculations of thermal cycles and fusion zone geometry [1-5]. In many simple systems, the computed thermal cycles have been used to quantitatively understand weld metal composition and phase composition, grain structure and inclusion structure. Capabilities to quantitatively understand geometry, composition and structure of welds in simple systems have provided hope that that one day

welding engineers may be able to use numerical models to tailor weldment characteristics [5-10] to meet specifications. In reality, the numerical heat transfer and fluid flow codes for fusion welding have so far been used mostly as a research tool rather than in the industry. There are several reasons for the restricted use of these advanced tools. An important difficulty is the need for several input parameters that cannot be easily specified.

Current computer models for the calculation of heat transfer and fluid flow in fusion welding require many input parameters to define the welding system such as the system geometry, welding variables, and thermophysical data. Several of these parameters such as the welding current, voltage and welding speed can be easily specified with a reasonable degree of certainty. However, the arc efficiency, effective thermal conductivity and the effective viscosity of the liquid metal in weld pool are the three important examples which are required for weld pool modelling [1, 11]. Values of these parameters are important, since they allow accurate modelling of the high rates

of transport of heat and mass in systems with strong fluctuating velocities that are inevitable in small weld pools with very strong convection currents [11-15]. Since fluctuating components of velocities exist in small weld pools with strong mean recirculating velocities, a regular practice has been to consider an enhancement in the values of liquid thermal conductivity and viscosity above their corresponding molecular values. Alternatively, the two-equation k-ε turbulence model [11-14] has also been applied in estimating effective viscosity and thermal conductivity in weld pool. However, the application of the two-equation k-ε turbulence model and the associated empirical constants, which was originally developed to model parabolic fluid flow in large systems (such as pipes), in small scale weld pools with elliptic flow is open to question. Thus, no unified basis to confidently prescribe the enhancements both for thermal conductivity and viscosity in weld pool based on scientific principles are available [15] to date. The present work attempts to outline a modelling procedure utilizing the power of a phenomenological heat transfer and fluid flow model and an optimisation algorithm to estimate these parameters as a function of power input. Due to narrow range of experimental data set, variation of arc efficiency, effective thermal conductivity and effective viscosity is considered to be linear with input power. So, now we need six variables i.e. constant terms and the slopes of the linear functions to define the arc efficiency, effective thermal conductivity and effective viscosity. These unknown values can then be used in a numerical heat transfer and fluid flow model under similar welding conditions.

Two interactive computational modules are embedded into the present smart model - one for the analysis of heat transfer and fluid flow in fusion welding and the other for the optimisation of the unknown parameters. The optimisation procedure attempts to estimate the unknown parameters by learning the sensitivity of the known variables with respect to the unknown parameters. The sensitivity terms have to be calculated by running the heat transfer and fluid flow model several times for small changes in the unknown parameters. The modelling procedure can be computationally very intensive and so far have been based on rather simple heat conduction equation, often utilizing Rosenthal's analytical

solution that completely ignored convection in the weld pool. Furthermore, the primary focus of these works was to determine the distribution of heat flux at the workpiece surface exposed to an arc or a laser beam from measured temperatures at several monitoring locations in the solid region. It seems that the adaptation of the simplified heat conduction equation in the previous work was mandated, at least to a large extent, because of the lack of fast computers and advanced software necessary to rigorously analyse heat and fluid flow in the weldment. With the advances in the computational hardware and software in recent years, it is now possible to undertake computationally intensive optimisation schemes that embody realistic three dimensional numerical heat transfer and fluid flow calculations. Since the optimisation routine principally learns from the results obtained from the actual weld pool modelling calculations, any simplification in the latter will have a strong influence on the accuracy and reliability of the estimated results of unknown parameters. Thus, the inclusion of a three-dimensional heat transfer and fluid flow model for weld pool simulation in the present work is certainly desirable if not necessary. Furthermore, the approach adopted here is inherently different from the neural network technique where the input and output variables are related through a set of hidden nodes and their relationships do not have to comply with any physical law. In contrast, when the optimisation algorithm embodies a heat transfer and fluid flow model, as adopted in the research reported in this paper, the input welding parameters and the output weld pool geometry are related by a phenomenological framework of the equations of conservation of mass, momentum and energy. In effect, the complete procedural scheme acts as a smart model that identifies important unknown parameters in an iterative manner starting from a set of their initial guessed values exploiting the phenomenological framework.

The goal of the present work is to estimate the variation of efficiency, effective thermal conductivity and effective viscosity with input power through an inverse modelling approach which includes a combination of an optimisation algorithm, a heat transfer and fluid flow model and, a set of experimentally measured weld pool penetration, throat and the leg length. Table 1 presents the

Table 1 – Welding conditions used in the experiments

Case No.	Contact tube to workpiece distance (CTWD) (mm)	Wire feeding rate (mm/s)	Travel speed (mm/s)	Voltage (V)	Estimated current (A)
1	22.2	169.3	4.2	31	312.0
2	22.2	211.7	6.4	31	362.0
3	22.2	169.3	6.4	33	312.0
4	22.2	211.7	4.2	33	362.0
5	28.6	169.3	6.4	31	286.8
6	28.6	169.3	4.2	33	286.8
7	28.6	211.7	4.2	31	331.4
8	28.6	211.7	6.4	33	331.4

Polarity: direct current electrode positive (DCEP).
Joint type: fillet joint, flat position, 90 degree joint angle, and no root gap.
Electrode type: 1.32 mm (0.052 inch) diameter solid wire.
Base metal: ASTM A-36 mild steel.
Shielding gas: Ar – 10 % CO_2.

experimentally measured values used in this work. The optimisation algorithm minimizes the error between the predicted and the experimentally observed penetration, throat and the leg length during the GMAW process by considering the sensitivity of the weld penetration, throat and the leg length to each of the unknown parameters. The Levenberg-Marquardt and two versions of conjugate gradient method (i.e., Fletcher-Reeves and Polak-Ribiere) of non-linear parameter optimisation are used to estimate these unknown parameters with a well tested three-dimensional numerical heat and fluid flow model.

2 MODEL DESCRIPTION

2.1 Modelling of heat transfer and fluid flow during GMA fillet welding

The heat transfer and fluid flow model takes into account the liquid metal convection in the weld pool, the complex fillet joint geometry, the deformation of the weld pool top surface, additions of the filler metal, and the heat transfer by metal droplets. The driving forces for weld pool convection include the surface tension gradient, the electromagnetic force and the buoyancy (gravitational) force. The complicated physical domain is transformed into a simple rectangular computational domain. The transformed governing equations are then discretized and solved in the computational domain using control volume method and a modified SIMPLE algorithm. The output from the model includes temperature and velocity fields, thermal cycles, fusion zone geometry and the solidified geometry of the weld reinforcement. More details about the numerical model are available in the literature [1, 16]. Only salient features are summarized below.

2.1.1 Governing equations

By using a coordinate system attached to the heat source, the welding problem is assumed to be at steady state [1]. Therefore, the heat transfer and fluid flow during welding can be calculated by solving the following governing equations [1, 16].

$$\frac{\partial u_i}{\partial x_i} = 0 \tag{1}$$

$$\rho \frac{\partial(u_i u_j)}{\partial x_i} = \frac{\partial}{\partial x_i}\left(\mu \frac{\partial u_i}{\partial x_i}\right) + S_j \tag{2}$$

$$\rho \frac{\partial(u_i h)}{\partial x_i} = \frac{\partial}{\partial x_i}\left(\alpha \frac{\partial h}{\partial x_i}\right) - \rho L \frac{\partial(u_i f_1)}{\partial x_i} - \rho U_w \frac{\partial h}{\partial x_1} - \rho U_w L \frac{\partial f_1}{\partial x_1} + S_v \tag{3}$$

Equations (1), (2) and (3) are the continuity, momentum conservation and energy conservation equations, respectively.

In these equations:

subscripts i and j indicate the coordinate direction (i, j = 1, 2 and 3),
x is the distance,
u is the melt velocity,
ρ is the density,

μ is the viscosity,
S_j is the source term for j-th momentum equation,
h is the sensible heat,
α is the thermal diffusion coefficient (defined as $\alpha = k/C_p$, where k is the thermal conductivity and C_p is the specific heat),
U_w is the material moving speed (parallel to the positive x direction, i.e., I = 1 direction),
L is the latent heat of fusion,
S_v is a source term accounting for the additional heat from metal droplets.

In equation (2), the source term S_j is given as:

$$S_j = -\frac{\partial p}{\partial x_j} - \rho U_w \frac{\partial u_j}{\partial x_1} - C\left(\frac{(1 - f_\ell)^2}{f_\ell^3 + B}\right)u_j + F_j^e + F_j^b \tag{4}$$

where

p represents pressure,
f_ℓ is the liquid metal fraction, and
F_j^e and F_j^b correspond to the electromagnetic and buoyancy forces in the j-th direction, respectively.

Details about the calculation of the electromagnetic and buoyancy source terms are available in the literature [1, 16, 17]. In equation (4), the third term represents the frictional dissipation in the mushy zone according to the Carman-Kozeny approximation [18], where B and C are two constants. The liquid metal fraction, f_ℓ, is assumed to vary linearly with temperature:

$$f_\ell = \begin{cases} 1 & T \geq T_\ell \\ \dfrac{T - T_s}{T_\ell - T_s} & T_s < T < T_\ell \\ 0 & T \leq T_s \end{cases} \tag{5}$$

where T_ℓ and T_s are the liquidus and solidus temperature of the material, respectively.

2.1.2 Coordinate transformation

Much of previous research to understand welding processes through numerical heat transfer and fluid flow calculations have focused mainly on simple systems such as butt welds. Regular Cartesian or Cylindrical grid system is conveniently employed in the numerical solution of governing equations. For fillet welding, accurate solution of heat transfer and fluid flow with a deformable weld pool surface and complex joint geometry desires the use of non-orthogonal deformable curvilinear grid system. Therefore, in the present work, the governing equations are transformed from the Cartesian to curvilinear coordinate system. Figure 1 shows the transformation from the L-shape physical domain denoted by (x, y, z) to a simple rectangular computational domain represented by (ξ, η, ζ), where the transformed governing equations were discretized and numerically solved. As shown in this figure, only the z coordinate in the physical domain is transformed into the ζ coordinate in the computational domain, while ξ and η coordinates remain the same as x and y coordinates, respectively. For clarity, subscripts x, y, z, ξ, η and ζ are used to represent corresponding partial derivatives in the following discussion. For example, symbols ξ_x and h_η represent the partial derivatives $\partial \xi / \partial x$ and $\partial h / \partial \eta$, respectively. Using the Chain rule [19, 20], the governing equations (1), (2)
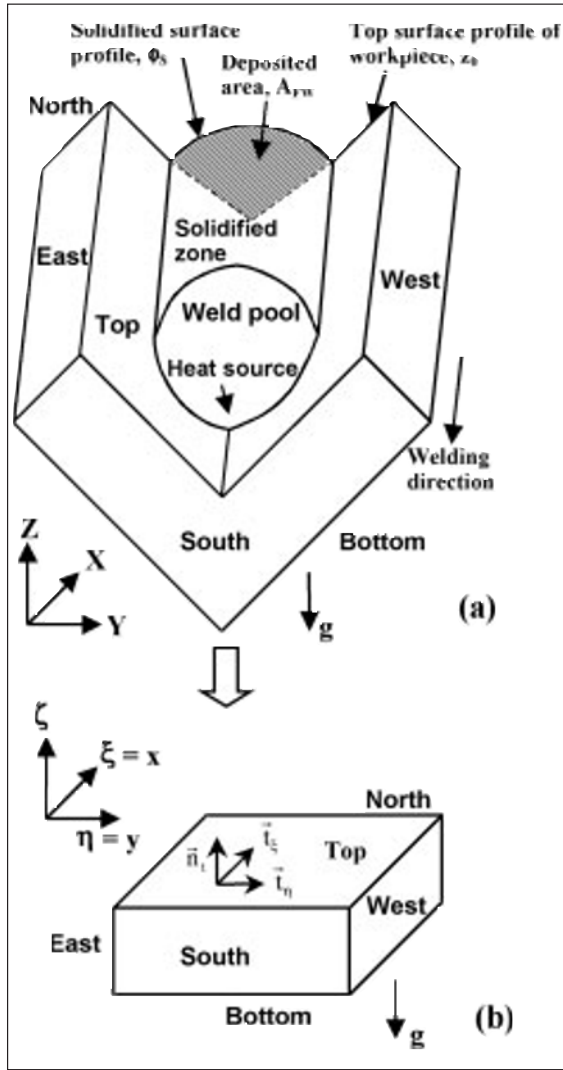
Symbols $\vec{n}_t$, $\vec{t}_\xi$ and $\vec{t}_\eta$ are the unit normal and tangential vectors to the top surface. The shadowed area, A_{FW}, is equal to the amount of fed wire per unit length.

**Figure 1 – Schematic plot showing the coordinate transformation from the physical (x, y, z) to the computational domain (ξ, η, ζ)
(a) Physical domain,
and (b) Computational domain**

and (3) are transformed into equations (6), (7) and (8), respectively, in the curvilinear coordinate [1, 16].

$$\frac{\partial U}{\partial \xi} + \frac{\partial V}{\partial \eta} + \frac{\partial W}{\partial \zeta} = 0 \tag{6}$$

$$\rho \left[\frac{\partial(Uu)}{\partial \xi} + \frac{\partial(Vu)}{\partial \eta} + \frac{\partial(Wu)}{\partial \zeta} \right] = \frac{\partial}{\partial \xi} \left[\mu \left(z_\zeta \frac{\partial u}{\partial \xi} - z_\xi \frac{\partial u}{\partial \zeta} \right) \right]$$
$$+ \frac{\partial}{\partial \eta} \left[\mu \left(z_\zeta \frac{\partial u}{\partial \eta} - z_\eta \frac{\partial u}{\partial \zeta} \right) \right] \tag{7}$$
$$+ \frac{\partial}{\partial \zeta} \left[\mu \left(- z_\xi \frac{\partial u}{\partial \xi} - z_\eta \frac{\partial u}{\partial \eta} + q_{33} \frac{\partial u}{\partial \zeta} \right) \right] - \left(z_\zeta \frac{\partial p}{\partial \xi} - z_\xi \frac{\partial p}{\partial \zeta} \right)$$
$$- \rho U_w \left(\frac{\partial(z_\xi u)}{\partial \xi} - \frac{\partial(z_\xi u)}{\partial \zeta} \right) - C \left(\frac{(1 - f_\ell)^2}{f_\ell^3 + B} \right) z_\zeta u + z_\zeta F_x^e + z_\zeta F_x^b$$

$$\rho \left[\frac{\partial(Uh)}{\partial \xi} + \frac{\partial(Vh)}{\partial \eta} + \frac{\partial(Wh)}{\partial \zeta} \right] = \frac{\partial}{\partial \xi} \left[\alpha \left(z_\zeta \frac{\partial h}{\partial \xi} - z_\xi \frac{\partial h}{\partial \zeta} \right) \right]$$
$$+ \frac{\partial}{\partial \eta} \left[\alpha \left(z_\zeta \frac{\partial h}{\partial \eta} - z_\eta \frac{\partial h}{\partial \zeta} \right) \right] \tag{8}$$
$$+ \frac{\partial}{\partial \zeta} \left[\alpha \left(- z_\xi \frac{\partial h}{\partial \xi} - z_\eta \frac{\partial h}{\partial \eta} + q_{33} \frac{\partial h}{\partial \zeta} \right) \right] - \rho U_w \left[\frac{\partial(z_\xi h)}{\partial \xi} - \frac{\partial(z_\xi h)}{\partial \zeta} \right]$$
$$- \rho L \left[\frac{\partial(Uf_\ell)}{\partial \xi} + \frac{\partial(Vf_\ell)}{\partial \eta} + \frac{\partial(Wf_\ell)}{\partial \zeta} \right] - \rho U_w L \left[\frac{\partial(z_\xi f_\ell)}{\partial \xi} - \frac{\partial(z_\xi f_\ell)}{\partial \zeta} \right] + z_\zeta S_v$$

where

u, v and w are Cartesian velocity components along the x, y and z directions, respectively, and
U, V and W are the contravariant velocity components in the ξ, η, and ζ directions, respectively.

The transformation coefficients are expressed as [1,16]:

$$\begin{bmatrix} \xi_x & \xi_y & \xi_z \\ \eta_x & \eta_y & \eta_z \\ \zeta_x & \zeta_y & \zeta_z \end{bmatrix} = \begin{bmatrix} 1 & 0 & 0 \\ 0 & 1 & 0 \\ -Jz_\xi & -Jz_\eta & J \end{bmatrix} \tag{9}$$

where

J is the Jacobian of the transformation and is given as $J = 1 / z_\zeta$.

Coefficient q_{33} is defined as $q_{33} = J (z_\xi^2 + z_\eta^2 + 1)$. The contravariant velocity components U, V and W are related to the Cartesian velocity components u, v and w by the following equation.

$$U = \frac{\xi_x u}{J} + \frac{\xi_y v}{J} + \frac{\xi_z w}{J} = z_\zeta u \tag{10}$$

$$V = \frac{\eta_x u}{J} + \frac{\eta_y v}{J} + \frac{\eta_z w}{J} = z_\zeta v$$

$$W = \frac{\zeta_x u}{J} + \frac{\zeta_y v}{J} + \frac{\zeta_z w}{J} = - z_\xi u - z_\eta v + w$$

2.1.3 Boundary conditions

The velocities at the weld pool top surface are given as:

$$\vec{v} \cdot \vec{n}_t = 0 \tag{11a}$$

$$\mu \nabla(\vec{v} \cdot \vec{t}_\xi) \cdot \vec{n}_t = f_\ell \left(\frac{d\gamma}{dT} \right) \nabla T \cdot \vec{t}_\xi \tag{11b}$$

$$\mu \nabla(\vec{v} \cdot \vec{t}_\eta) \cdot \vec{n}_t = f_\ell \left(\frac{d\gamma}{dT} \right) \nabla T \cdot \vec{t}_\eta \tag{11c}$$

where

$\vec{v}$ is the liquid metal velocity,
$d\gamma/dT$ is the temperature coefficient of surface tension,
$\vec{n}_t$ is the local unit normal vector to the top surface, and
$\vec{t}_\xi$ and $\vec{t}_\eta$ are local unit tangential vectors to the top surface along the ζ and η directions, respectively.

Equation (11a) indicates that the normal velocity to the weld pool top surface is zero, while equations (11b) and (11c) represent the Marangoni sheer stress at the top surface. As shown in Figure 1 (b), the normal and tangential vectors to the weld pool top surface are given as:

$$\vec{n}_t = \frac{\zeta_x \vec{i} + \zeta_y \vec{j} + \zeta_z \vec{k}}{\sqrt{\zeta_x^2 + \zeta_y^2 + \zeta_z^2}}, \quad \vec{t}_\xi = \frac{x_\xi \vec{i} + y_\xi \vec{j} + z_\xi \vec{k}}{\sqrt{x_\xi^2 + y_\xi^2 + z_\xi^2}},$$

$$\vec{t}_\eta = \frac{x_\eta \vec{i} + y_\eta \vec{j} + z_\eta \vec{k}}{\sqrt{x_\eta^2 + y_\eta^2 + z_\eta^2}} \tag{12}$$

where

$\vec{i}$, $\vec{j}$ and $\vec{k}$ are the unit vectors along x, y and z directions, respectively.

The liquid metal velocity at all other surfaces, i.e., bottom, east, west, south and north surfaces, are equal to zero.

The heat flux from the arc is assumed to be a Gaussian distribution at the weld top surface. As shown in Figure 1 (a), the heat flux at the top surface, F_t, is given as [1, 16]:

$$\alpha \nabla h \cdot \vec{n}_t = F_t = \frac{IV\eta}{2\ \pi r_b^2} exp\left(-\frac{x_h^2 + y_h^2}{2\ r_b^2}\right)(\vec{k} \cdot \vec{n}_t) - \sigma\varepsilon(T^4 - T_a^4)$$

$$- h_c(T - T_a) \qquad (13)$$

where

I is the current,
V is the voltage,
η is the power efficiency,
r_b is the heat distribution parameter,
x_h and y_h are the x and y distances to the arc axis, respectively,
σ is the Stefan-Boltzmann constant,
ε is the emissivity,
h_c is the convective heat transfer coefficient, and
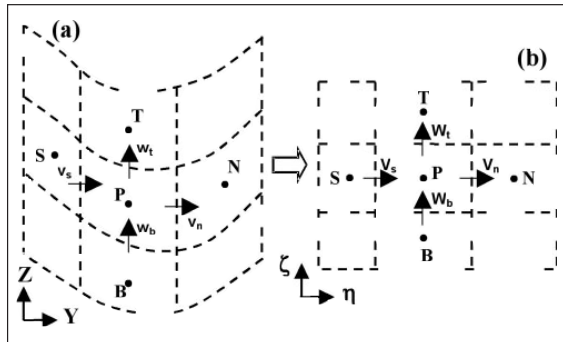T_a is the ambient temperature (a value of 298 K is used).

For the bottom surface, the heat flux, F_b, is given as:

$$\alpha \nabla h \cdot \vec{n}_b = F_b = h_c\ (T - T_a) \qquad (14)$$

where

$\vec{n}_b$ is a unit normal vector to the bottom surface.

The temperatures at other surfaces, i.e., east, west, south, and north surfaces are set to the ambient temperature.

Dashed lines represent control volume's interfaces.
Solid dots indicate scalar grid points.
Symbols W, E, S, N, B, T are the east, west south, north, bottom and top neighbours of the grid point P, respectively.
Symbols s, n, b, t are the south, north, bottom and top interfaces of the control volume P.

Figure 2 – Grid system in the physical and computational domains
(a) A YZ plane in the physical domain, and
(b) The corresponding ηζ plane in the computational domain

2.1.4. Grid system and discretization of the governing equations

The transformed governing equations, i.e., (6), (7) and (8), are discretized using the control volume method, where the computational domain is divided into small rectangular control volumes, as shown in Figure 2. A scalar grid point is located at the centre of each control volume, storing the values of scalar quantities such as pressure and enthalpy. Velocity components lie at the control volume faces, staggered with respect to scalar locations. For example, both Cartesian v velocity and contravariant V velocity are placed at the south and north faces of a control volume P, as shown in Figure 2. Thus, the control volumes for vectors are different from those for scalars. Such an arrangement is extensively used in orthogonal coordinates to prevent the decoupling of the velocity and pressure fields [21]. Discretized equations for a variable are formulated by integrating the corresponding governing equation over the control volumes in the computational domain. A power-law based scheme is used to describe the convective flux at the control volume faces. The final expression can be written in the following general form as [21]:

$$a_P\phi_P = a_E\phi_E + a_W\phi_W + a_N\phi_N + a_S\phi_S + a_T\phi_T + a_B\phi_B + b \quad (15)$$

where

a_E, a_W, etc., denote the combined convection-diffusion coefficients, and
b includes all the source terms.

A modified Semi-Implicit Algorithm for Pressure Linked Equations (SIMPLE) is used to solve the discretized equations [16]. The modification takes into account the main feature in the transformed governing equations in the curvilinear coordinate system, i.e., a mixed Cartesian-contravariant velocity components.

2.1.5 Heat transfer from metal droplets

An important feature of the GMA welding is the finger penetration which is mainly caused by the transfer of heat from the superheated metal droplets into the weld pool. In the present work, the droplet heat transfer is effectively simulated by incorporating a time-averaged volumetric heat source term (S_v) in the energy conservation equation. This volumetric heat source is characterized by its radius, height and power density. Details about the calculation of the volumetric heat source based on the available knowledge base of the interaction between metal droplets and the weld pool for various welding conditions are available in reference [1].

2.1.6 Calculation of the weld pool top surface profile

During GMA fillet welding, the weld pool top surface under the electrode is depressed by the arc force. Furthermore, the addition of filler metal also deforms the weld pool. Therefore, the pool top surface is not flat and the surface profile needs to be determined. In the present work, an energy minimization method was used. The total energy to be minimized includes the surface energy due to the change in area of the pool surface,

the potential energy in the gravitational field and the work performed by the arc pressure displacing the pool surface. Detailed procedure for the calculation of the free surface profile is available in the literature [1], and only salient features are presented here.

The following two equations are solved to obtain the weld pool surface profile.

$$\gamma \left\{ \frac{(1 + \phi_y{}^2)\phi_{xx} - 2\,\phi_x\phi_y\phi_{xy} + (1 + \phi_x{}^2)\,\phi_{yy}}{(1 + \phi_x{}^2 + \phi_y{}^2)^{3/2}} \right\} = \rho g\phi + P_a + \lambda \quad (16)$$

$$\int(\phi_s - z_0)dy - \frac{\pi r_w{}^2 w_f}{U_w} = 0 \quad (17)$$

In equation (16):

γ is the surface tension,
P_a is the arc pressure distribution at the pool top surface, and
λ is the Lagrange multiplier.

In equation (17):

r_w, w_f and U_w are the wire radius, wire feeding rate and the welding speed, respectively, and
ϕ_s is the solidified surface profile,
z_0 is the z location of the workpiece top surface, as shown in Figure 1.

Equation (16) represents the static force balance at the pool top surface, while equation (17) defines a constraint condition that the deposited area, A_{FW}, at a solidified cross section of the fillet weld is equal to the amount of fed wire per unit length, as shown in Figure 1.

The pressure distribution at the top surface, P_a, is given as:

$$P_a = \frac{F}{2\,\pi\sigma_p{}^2} \exp\left(-\frac{x_h{}^2 + y_h{}^2}{2\sigma_p{}^2}\right) \quad (18)$$

where

F is the total arc force,
σ_p is the distribution parameter for arc pressure, and
x_h and y_h are the x and y distances to the arc axis, respectively.

The values of F and σ_p were calculated based on the extensive experimental work of Lin and Eagar [22] as:

$$F = -0.04791 + 0.0002447 \times I \; (N) \quad (19)$$

$$\sigma_p = 1.4875 + 0.00123 \times I \; (mm) \quad (20)$$

where

I is the welding current in Ampere.

2.1.7 Overall solution procedure

The governing equations are solved "simultaneously" to obtain the temperature and velocity fields and the free surface profile. First, the modified SIMPLE algorithm is used to calculate the temperature and velocity fields. Then, the free surface profile is calculated based on the temperature field obtained in the previous step. After the solution of the free surface profile, the z locations of grids are adjusted to fit the surface profile, and the temperature and velocity fields are then re-calculated in the fitted grid system. The calculation procedure is repeated until converged temperature and velocity fields and free surface profile are obtained.

A $72 \times 66 \times 47$ grid system was used and the corresponding solution domain had dimensions of 450 mm in length, 108 mm in width and 18 mm in depth. Spatially non-uniform grids with finer grids near the heat source were used for maximum resolution of variables. The calculations normally converged within 5 000 iterations, which took about 30 minutes in a PC with 2.8 GHz Intel P4 CPU and 512 Mb PC2700 DDR-SDRAM memory. Comparing with the heat transfer model [1] which converges in 4 000 iterations (about 6 minutes), the heat transfer and fluid flow calculation is much more computationally intensive.

2.2 Inverse modelling

Inverse modelling provides the estimation of unknown welding parameters using the measurements of weld features like, the actual throat, leg length and penetration in the fillet weld. The inverse problem is often difficult to solve because it is a mathematically ill-posed problem [23-29], and small perturbations in the observed parameters functions may result into large changes in the corresponding solutions and requires special numerical techniques to stabilize [23-29] the results of the calculations. In general, inverse problems require more computation time than the corresponding direct approaches since it usually involves an iterative procedure involving multiple computations of the direct problem.

Inverse model involves the minimization of an objective function that depicts the difference between the computed and measured values. For example, if the penetration, throat and the leg length of the fusion zone are of interest, an objective function, O(f), can be defined as follows:

$$O(f) = \sum_{m=1}^{M} (p_m^e - p_m^c)^2 + \sum_{m=1}^{M} (t_m^e - t_m^c)^2 + \sum_{m=1}^{M} (l_m^e - l_m^c)^2 \quad (21)$$

where

p_m^c, t_m^c and l_m^c are the penetration, actual throat and the leg length of the weld pool calculated by the numerical heat transfer and fluid flow model, respectively and, p_m^e, t_m^e and l_m^e are the corresponding experimentally determined values of these two variables.

The penetration, actual throat and leg length in a GMAW fillet weld are defined in Figure 3. The subscript m in equation (21) corresponds to a specific weld in a set of M welds. Equation (21) bears a strong resemblance to the functional form of least square technique for the minimization of error.

Often an experiment is repeated to determine the standard deviation, σ_m, in measurements. These standard deviations can be included in the objective function such that more reliable measurements with small standard deviations get a higher weight than less reliable measurements that are characterized by relatively large standard deviations. A weight factor can also be assigned with the measured quantities if they represent different measurement scale or the physical dimension. The
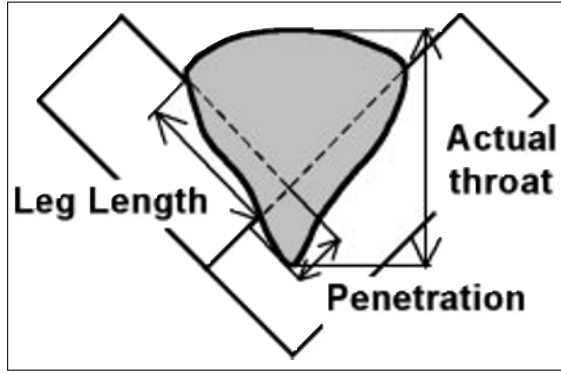
Figure 3 – Nomenclature of the weld geometry in GMAW fillet weld

objective function, O(f), can now be redefined as follows where every weld is fabricated a multiple number of times.

$$O(f) = \sum_{m=1}^{M} \frac{(p_m^e - p_m^c)^2}{w_p \sigma_m^2} + \sum_{m=1}^{M} \frac{(t_m^e - t_m^c)^2}{w_t \sigma_m^2} + \sum_{m=1}^{M} \frac{(l_m^e - l_m^c)^2}{w_l \sigma_m^2} \quad (22)$$

where

w_p, w_t and w_l represent the weight factor assigned to penetration, throat and leg length respectively.

In equations (21) and (22), f refers to a set of six unknown non-dimensional parameters, f_1, f_2, f_3, f_4, f_5 and f_6 of the constant terms (i.e. A, B, C, D, E and F) of the assumed linear functions of efficiency, η, effective thermal conductivity, k_{eff}, and effective viscosity, μ_{eff}, with the non-dimensional input power, P_i^*, in the following manner:

$$\{f\} = \{f_1\ f_2\ f_3\ f_4\ f_5\ f_6\} = \{A\ B\ C/k_L\ D/k_L\ E/\mu_L\ F/\mu_L\} \quad (23)$$

$$\eta = A + B \cdot P_{in}^* \quad (24)$$

$$k_{eff} = C + D \cdot P_i^* \quad (25)$$

$$\mu_{eff} = E + F \cdot P_i^* \quad (26)$$

$$P_{in}^* = \frac{IV / (\pi r_w^2 w_f)}{[\rho c_p (T_\ell - T_a) + \rho L]} \quad \text{and} \quad P_i^* = \frac{IV / (\pi r_b^2 U_w)}{[\rho c_p (T_\ell - T_a) + \rho L]} \quad (27)$$

where

k_L is the conductivity of the liquid material,
μ_L is the viscosity of the liquid material,
I is the current,
V is the voltage,
r_w is the wire radius,
w_f is the wire feeding rate,
ρ is the density,
c_p is the specific heat,
T_l is the liquidus temperature,
T_a is the ambient temperature,
L is the latent heat of the alloy,
r_b is the arc radius and
U_w is the welding speed.

In equation (24), input power is non-dimensionalised with wire feeding rate and wire radius because if any of these two parameters is large, more power will be consumed in melting the wire. Therefore, less power will go to the workpiece in the form of arc. While, in case of effective thermal conductivity and effective viscosity,

input power is non-dimensionalised with respect to the welding speed and the arc radius. The reason is that with high torch speed or the arc radius, the input power will be distributed in a larger area which will reduce the effect of input power on the turbulence behaviour in the weld pool. This reduction in turbulence behaviour will lead to less increase in effective thermal conductivity and viscosity.

Evidently, O(f) is a function of f since O(f) contains variables p_m, t_m and l_m, which are dependent on the parameters included in f. Assuming that O(f) is continuous and has a minimum value, the optimum values of the six unknowns are obtained by differentiating equation (21) with respect to the six unknown parameters and equating each derivative to zero:

$$[\nabla O(f^k)]_{i=1,6} = \left(\frac{\partial O(f)}{\partial f_i}\right)_{i=1,6} = -2 \left[\sum_{m=1}^{M} \frac{(p_m^e - p_m^c)}{w_p \sigma_m^2} \frac{\partial p_m^c}{\partial f_i} \right.$$
$$\left. + \sum_{m=1}^{M} \frac{(t_m^e - t_m^c)}{w_t \sigma_m^2} \frac{\partial t_m^c}{\partial f_i} + \sum_{m=1}^{M} \frac{(l_m^e - l_m^c)}{w_l \sigma_m^2} \frac{\partial l_m^c}{\partial f_i} \right]_{i=1,6} = 0 \quad (28)$$

where

f_i represents any one of the six unknowns in f.

Equation (28) contains partial derivatives of weld penetration, actual throat and leg length with respect to all six unknown parameters. These partial derivatives are generally referred as sensitivity of the computed weld penetration, actual throat and leg length with respect to the unknown parameters. The values of these sensitivity terms are computed numerically by running the numerical heat transfer and fluid flow code and subsequently calculating the derivatives. For example, the sensitivity of non-dimensional penetration, p_m^c, with respect to variable 4, f_4, is calculated from the following relation:

$$\frac{\partial p_m^c}{\partial f_4} = \frac{p_m^c (f_1, f_2, f_3, f_4 + \Delta f_4, f_5, f_6) - p_m^c (f_1, f_2, f_3, f_4, f_5, f_6)}{\Delta f_4} \quad (29)$$

where

Δf_4 is very small compared with f_4.

The equation (29) depicts that each sensitivity term need two executions of the direct numerical analysis. Now, equation (28) calls for the calculated values of p_m^c, t_m^c and l_m^c to be very close to the corresponding experimental values of p_m^e, t_m^e and l_m^{es} for all M sample welds. Since p_m^c, t_m^c and l_m^c in equation (28) are obtained from the solution of the direct numerical heat and fluid flow model for a certain set of six unknown parameters, and these unknown parameters do not explicitly appear in equation (28), this equation cannot provide a direct solution for the desired unknown parameters. These sensitivity terms can be written in a matrix form, known as sensitivity matrix, J(f). The elements of the sensitivity matrix, i.e. sensitivity coefficients, J_{ij}, are defined as:

$$J_{ij} = \frac{\partial (p_i^c)^k}{\partial f_j} + \frac{\partial (t_i^c)^k}{\partial f_j} + \frac{\partial (l_i^c)^k}{\partial f_j} \quad (30)$$

where

i = 1 to M and
j = 1 to 6.

For the minimization of least-square objective function [i.e. equation (22)], Levenberg-Marquardt (LM) method

and two different modifications of the conjugate gradient method suggested by Fletcher-Reeves and Polak-Ribiere are used for the analysis. These methods differ in calculation of step size (i.e. increment in the unknown parameter) and direction of descent which is physical representation of the relative change in the unknown parameters.

2.2.1 Levenberg-Marquardt method

To calculate the step size in LM method, the dependent variables p_m, t_m, and l_m can be expanded using the Taylor's series to explicitly contain values of increments and unknown parameters i.e. f_1, f_2, f_3, f_4, f_5 and f_6. The higher derivative terms in the Taylor's series can be dismissed because these are very small compared to the term involving the first derivative. So, for the variable p_m^c the expansion takes the following form:

$$(p_m^c)^{k+1} = (p_m^c)^k + \frac{\partial(p_m^c)^k}{\partial f_1}\Delta f_1^k + \frac{\partial(p_m^c)^k}{\partial f_2}\Delta f_2^k + \frac{\partial(p_m^c)^k}{\partial f_3}\Delta f_3^k$$

$$+ \frac{\partial(p_m^c)^k}{\partial f_4}\Delta f_4^k + \frac{\partial(p_m^c)^k}{\partial f_5}\Delta f_5^k + \frac{\partial(p_m^c)^k}{\partial f_6}\Delta f_6^k \qquad (31)$$

where

Δf_1^k, Δf_2^k, Δf_3^k, Δf_4^k, Δf_5^k and Δf_6^k are the unknown increments in f_1, f_2, f_3, f_4, f_5 and f_6.

Superscripts k and k+1, represent the values at the kth and $(k + 1)^{th}$ iterations, respectively. All other terms on the right hand side of equation (31) are considered to be known. The value of p_m^c at the end of $(k + 1)^{th}$ iteration i.e. $(p_m^c)^{k+1}$, is unknown since Δf_1^k, Δf_2^k, Δf_3^k, Δf_4^k, Δf_5^k and Δf_6^k, and hence, f_1, f_2, f_3, f_4, f_5 and f_6 after $(k + 1)^{th}$ iteration are unknown. It should be noted here that p_m^c is always considered to be evaluated through a direct numerical solution using a corresponding set of f_1, f_2, f_3, f_4, f_5 and f_6 and other known parameters. The terms in equation (28) represents the k + 1 iteration terms which are unknown. So these terms can be rewritten as k^{th} iteration terms using equation (31). Substituting equation (30) in equation (28) and removing the second derivative terms will convert equation (28) to following form:

$$[S]\{\Delta f^k\} = \{S^*\} \qquad (32)$$

with [S] as $N \times N$ matrix containing sensitivity terms, Δf^k as $N \times 1$ matrix and S* as $N \times 1$ matrix where N represents the number of unknown variables i.e. 6. The elements of matrix [S], i.e.,

$$[S] = \begin{bmatrix} S_{11} & S_{12} & S_{13} & S_{14} & S_{15} & S_{16} \\ S_{21} & S_{22} & S_{23} & S_{24} & S_{25} & S_{26} \\ S_{31} & S_{32} & S_{33} & S_{34} & S_{35} & S_{36} \\ S_{41} & S_{42} & S_{43} & S_{44} & S_{45} & S_{46} \\ S_{51} & S_{52} & S_{53} & S_{54} & S_{55} & S_{56} \\ S_{61} & S_{62} & S_{63} & S_{64} & S_{65} & S_{66} \end{bmatrix} \qquad (33)$$

can be written as:

$$S_{ij} = \sum_{m=1}^{8}\left(\frac{1}{w_p\sigma_m^2}\frac{\partial(p_m^c)^k}{\partial f_i}\frac{\partial(p_m^c)^k}{\partial f_j} + \frac{1}{w_t\sigma_m^2}\frac{\partial(t_m^c)^k}{\partial f_i}\frac{\partial(t_m^c)^k}{\partial f_j}\right.$$

$$\left. + \frac{1}{w_l\sigma_m^2}\frac{\partial(l_m^c)^k}{\partial f_i}\frac{\partial(l_m^c)^k}{\partial f_j}\right);$$

for i, j = 1 to 6 \qquad (34)

The indices i and j refer to the number of unknown parameters. Furthermore,

$$\{S^*\} = \begin{Bmatrix} S_1^{ptl} \\ S_2^{ptl} \\ S_3^{ptl} \\ S_4^{ptl} \\ S_5^{ptl} \\ S_6^{ptl} \end{Bmatrix} \qquad (35)$$

with

$$S_i^{ptl} = \sum_{m=1}^{8}\left(\frac{\partial(p_m^c)^k}{\partial f_i}\left(\frac{p_m^e - (p_m^c)^k}{w_p\sigma_m^2}\right) + \frac{\partial(t_m^c)^k}{\partial f_i}\left(\frac{t_m^e - (t_m^c)^k}{w_t\sigma_m^2}\right)\right.$$

$$\left. + \frac{\partial(l_m^c)^k}{\partial f_i}\left(\frac{l_m^e - (l_m^c)^k}{w_l\sigma_m^2}\right)\right);$$

for i = 1 to 6 \qquad (36)

The unknown matrix $\{\Delta f^k\}$ in equation (32) has also to be modified as:

$$\{\Delta f^k\} = \begin{Bmatrix} \Delta f_1^k \\ \Delta f_2^k \\ \Delta f_3^k \\ \Delta f_4^k \\ \Delta f_5^k \\ \Delta f_6^k \end{Bmatrix} \qquad (37)$$

The expression in equation (37) should now be treated as,

$$f_1^{k+1} = f_1^k + \Delta f_1^k$$
$$f_2^{k+1} = f_2^k + \Delta f_2^k$$
$$f_3^{k+1} = f_3^k + \Delta f_3^k$$
$$f_4^{k+1} = f_4^k + \Delta f_4^k \qquad (38)$$
$$f_5^{k+1} = f_5^k + \Delta f_5^k$$
$$f_6^{k+1} = f_6^k + \Delta f_6^k$$

Furthermore, the sensitivity terms such as

$$\frac{\partial(p_m^c)^k}{\partial f_i} \text{ or } \frac{\partial(t_m^c)^k}{\partial f_i} \text{ or } \frac{\partial(l_m^c)^k}{\partial f_i}$$

(for i = 1 to 6) in the equations (34) as well as in (36) often tend to be very small as the values of the unknown parameters f_1, f_2, f_3, f_4, f_5 and f_6 move close to the optimum values. As the optimum combination of the unknown parameters are reached, the individual influence of a specific parameter on the dependent variables, manifested by the sensitivity terms, may become very small or zero. Subsequently, the matrix [S] may tend to become a singular matrix and the inverse problem may become ill-conditioned. The matrix [S] can be null if any column of [S] can be expressed as a linear combination of other columns. To avoid any numerical instability, equation (32) is further modified following Levenburg-Marquardt method as:

$$([S] + \lambda^k\Omega^k)\{\Delta f^k\} = \{S^*\} \qquad (39)$$

where

λ^k is a scalar damping coefficient and usually taken as 0.001 and

Ω^k is the diagonal matrix.

The order of Ω^k is same as that of the matrix [S] and is defined as $\Omega^k = $ diag [S]. Thus the product $\lambda^k\,\Omega^k$ in equa-

tion (39) ensures that the left hand term in equation (39) will remain non-zero even if the determinant of the matrix [S] is zero. The damping parameter is generally made large at the beginning of the iterations, since the problem is generally ill-conditioned in the region around the initial guess in the iterative procedure, which can be quite far from the final solution. The parameter λ^k is then gradually decreased as the iteration procedure advances to the solution of the parameter estimation problem.

Algorithm:

1. Guess initial values of unknown variables set, f.

2. Compute objective function, O(f).

3. Choose a modest value for damping factor (λ), say $\lambda = 0.001$.

4. Solve for increment in unknown variables, Δf.

5. Evaluate O(f + Δf).

6. If O(f + Δf) $\geq$ O(f), increase λ by a factor of 10 (or any other substantial factor) and go back to step 4.

7. If O(f + Δf) < O(f), decrease λ by a factor of 10 (or any other substantial factor), update f.

8. Exit if stopping criteria is satisfied, otherwise go back to step 4.

The following stopping criteria suggested by Dennis and Schnabe [27] to stop the iterative procedure of the LM method is used in this paper.

1. $O(f^{k+1}) < \varepsilon_1$.

2. $\| S^* \| < \varepsilon_2$.

3. $\| f^{k+1} - f^k \| < \varepsilon_3$.

where

ε_1, ε_2 and ε_3 are user prescribed tolerances, and

$\| . \|$ is the vector Euclidean norm, i.e. $\| x \| = (x^T x)^{1/2}$, where the superscript T denotes the transpose.

The first criteria tests if the objective function is sufficiently small, which is going to be the neighbourhood of the solution for the problem. Similarly, second criteria checks if the norm of the gradient of O(f) is sufficiently small, since it is expected to vanish at the point where O(f) is minimum. Although such a condition of vanishing gradient is also valid for maximum and saddle points of the O(f), the LM method is very unlike to converge to such points [25, 30]. The third stopping criteria results from the fact that changes in the vector of parameters are very small when the method has converged. The use of a stopping criteria based on small changes of the least square norm O(f) could also be used, but with extreme caution. It may happen that the method stalls for a few iterations and then starts advancing to the point of minimum afterwards [26, 27].

2.2.2 Conjugate gradient method

Conjugate gradient method differs from LM method principally in the calculation of search step size and the direction of descent. In the iterative procedure of the conjugate gradient method, at each iteration a suitable step size is taken along a direction of descent in order to minimize the objective function. The direction of descent is obtained as a linear combination of the negative gradient direction at the current iteration with the direction of the descent of the previous iteration [31, 32]. This linear combination is such that the resulting angle between the direction of descent and the negative gradient direction is less than 90° and the minimization of the objective function is assured.

The iterative procedure of the Conjugate Gradient method for the minimization of the objective function is given by:

$$f_i^{k+1} = f_i^k - \beta^k d_i^k \quad \text{for i = 1 to 6} \tag{40}$$

where

β^k is the search step size;

k is the number of iterations and

d_i^k is the direction of descent for the ith variable.

The direction of descent for variable i, d_i^k, is a conjugation of its gradient direction, $\nabla O(f^k)_i$, and its direction of the descent of the previous iteration, d_i^{k-1} and is given as:

$$d_i^k = [\nabla O(f^k)]_i + \gamma^k d_i^{k-1} \quad \text{for i = 1 to 6} \tag{41}$$

where

γ^k is the conjugation coefficient.

Different expressions are available in the literature for the conjugate coefficient, γ^k. Fletcher and Reeves [30] suggested γ^k as:

$$\gamma^k = \frac{\sum_{i=1}^{N} [\nabla O(f^k)]_i^2}{\sum_{i=1}^{N} [\nabla O(f^{k-1})]_i^2} \quad \text{for k = 1, 2, ...; and } \gamma^0 = 0 \tag{42}$$

where

N is the number of unknown variables, i.e. 6. Polak-Ribiere [31] suggested expression for γ^k as:

$$\gamma^k = \frac{\sum_{i=1}^{N} [\nabla O(f_i^k)]_i [\nabla O(f_i^k) - \nabla O(f_i^{k-1})]_i}{\sum_{i=1}^{N} [\nabla O(f^{k-1})]_i^2}$$

for k = 1, 2, ...; and $\gamma^0 = 0$ \tag{43}

Here, $[\nabla O(f^k)]_i$ is the gradient directions of variable i evaluated at iteration k evaluated in equation (22). Either expression [equations (42) and (43)] for the computation of the conjugation coefficient γ^k assure that the angle between the direction of descent and the negative gradient direction is less than 90°, so that the objective function is minimized. If $\gamma^k = 0$ for all iterations k, the direction of descent becomes the gradient direction in equation (41) and the steepest-descent method is obtained.

The search step size, β^k, is obtained as the one which minimizes the objective function. Substituting the values of Taylor series expansion of the unknown parameters at iteration k+1 [i.e. equation (40) in equation (22)], and minimizing with respect to β^k, we get:

$$\beta^k = \frac{\sum\limits_{m=1}^{M} \left\{ \frac{(p_m^c - p_m^e)}{w_p \sigma_m^2} \left[\sum\limits_{i=1}^{N} \left(\frac{\partial p_m^c}{\partial f_i^k} \right) d_i^k \right] + \frac{(t_m^c - t_m^e)}{w_t \sigma_m^2} \left[\sum\limits_{i=1}^{N} \left(\frac{\partial t_m^c}{\partial f_i^k} \right) d_i^k \right] + \frac{(\ell_m^c - \ell_m^e)}{w_1 \sigma_m^2} \left[\sum\limits_{i=1}^{N} \left(\frac{\partial l_m^c}{\partial f_i^k} \right) d_i^k \right] \right\}}{\sum\limits_{m=1}^{M} \left[\sum\limits_{i=1}^{N} \left(\frac{\partial p_m^c}{\partial f_i^k} \right) d_i^k + \sum\limits_{i=1}^{N} \left(\frac{\partial t_m^c}{\partial f_i^k} \right) d_i^k + \sum\limits_{i=1}^{N} \left(\frac{\partial l_m^c}{\partial f_i^k} \right) d_i^k \right]^2} \tag{44}$$

After computing the sensitivity terms, the gradient direction, the conjugation coefficient and the search step size, the iterative procedure given by equation (40) is implemented until a stopping criterion is satisfied.

Algorithm:

1. Calculate the objective function, O(f) for the initial guesses of unknown variables, f.

2. Check the stopping criteria. Continue if not satisfied.

3. Compute the sensitivity matrix, J(f).

4. Compute the gradient direction, $\nabla O(f^k)_i$.

5. Evaluate the conjugate coefficient, γ^k.

6. Compute the direction of descent, d_i^k.

7. Compute the search step size, β^k.

8. Compute the new estimates for the unknown variables, f^{k+1}.

9. Increase the iteration no. and return to step 1.

In "chi-square objective function" the uncertainties associated with each data are required. If these values are not known in advance then it is assumed that all measurements have the same standard deviation, $\sigma_m = \sigma$, and the model does fit well with the data, then we can proceed by assigning an arbitrary constant like $\sigma = 1$ to all points [32]. It converts the objective function from chi-square function to a least square function.

3 RESULTS AND DISCUSSION

3.1 Calculations of heat transfer and fluid flow

As discussed in previously, the numerical heat transfer and fluid flow model was used as the direct model. The physical properties of the A-36 mild steel workpiece used in the calculations are given in Table 2. The numerical model provides detailed information of weld temperature distribution, veloci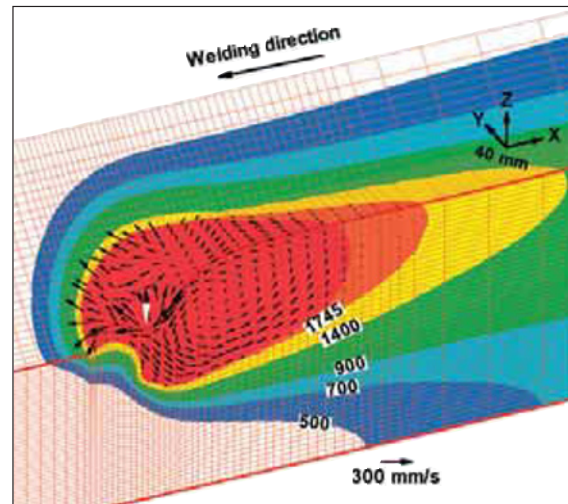ty field in the weld pool and sur-face profile for a given set of input parameters. Some salient findings of heat transfer and fluid flow calculations are briefly discussed below and more details are available in the reference [16].

3.1.1 Heat transfer and fluid flow in the fillet weld pool

The calculated temperature and velocity fields in a fillet weld are shown in Figure 4. The welding conditions used are those in case #4 shown in Table 1. For clarity, only half of the workpiece is shown, since the weld is symmetric about the central longitudinal plane containing the welding direction. As shown in this figure, the liquid metal motion is quite complicated due to the combined effect of the driving forces. The electromagnetic force plays a dominant role in driving the liquid metal flow in the weld pool. In the middle of the weld pool, the liquid metal is driven downwards by the electromagnetic force, and a major anticlockwise circulation loop is formed along the central longitudinal plane. On the other hand, at the top surface of the weld pool, the Marangoni shear stress drives the melt from the centre to the edge of the pool in the region close to the heat source, where the spatial variation of the surface temperature is relatively high. In the rear part of the weld pool, where the temperature gradient is relatively low, the effect of Marangoni shear stress is less strong than that of elec-

Table 2 – Physical properties of the A-36 mild steel workpiece used in the calculation

Physical property	Value
Liquidus temperature, T_L, (K)	1 785.0
Solidus temperature, T_S, (K)	1 745.0
Density of metal, ρ, (kg/m³)	7 200
Thermal conductivity of solid, k_S, (J/m.s.K)	21.0
Specific heat of solid, C_{PS}, (J/kg.K)	703.4
Specific heat of liquid, C_{PL}, (J/kg.K)	808.1
Surface tension of liquid metal (N/m)	1.2

All the temperatures are given in Kelvin.
The white arrow in the middle of the weld pool
indicates the location of the heat source.
The weld pool boundary is represented
by the 1 745 K isothermal line.
Welding conditions are the same as those in case #4.

Figure 4 – Calculated 3D temperature and velocity fields in a fillet weld

tromagnetic force. As a result, the liquid metal flows inward in the rear part of the pool.

3.1.2 Relative importance of convection and conduction in the heat transfer in the weld pool

During welding, the arc energy is carried away from the top surface of the weld pool to the surrounding solid region by both heat conduction and liquid metal convection. The rate of the heat flow determines not only the peak temperature and shape of the weld pool but also the temperature distribution in the heat-affected zone (HAZ). Therefore, it is of importance to understand the effect of conduction and convection on the heat dissipation in the weld pool. The relative importance of convection and conduction in the transfer of heat in the weld pool can be accessed from the value of the Peclet number (Pe), which is given by:

$$Pe = \frac{u_R \rho C_p L_R}{k} \qquad (45)$$

where

u_R and L_R are the characteristic velocity and length of the weld pool, respectively, and the symbols ρ, C_p and k have been defined earlier.

When Pe is large, which in physical terms means large liquid metal velocity, large weld pool, and poor thermal conductivity, the liquid metal convection significantly affects heat transfer in the weld pool. On the other hand, when Pe is small, say much less than unity, the conduction plays an important role in the heat dissipation in the weld pool.

For the fillet weld shown in Figure 4, if the average v velocity and the pool width are used as the characteristic velocity and length of the weld pool, respectively, the Peclet number is then calculated to be 120. Since the Peclet number is much larger than unity, the liquid metal convection plays a dominant role in the dissipation of heat in the weld pool.

3.1.3 Weld thermal cycles

The temperature field obtained from the calculation is at quasi-steady state, since the coordinate system is attached to the heat source moving at a constant welding speed. Therefore, the thermal cycles can be calculated by converting the x distance into time using the welding speed. Figure 5 shows the thermal cycles at the top surface of the fillet weld for case #2. Curve 1 is located in the FZ and curves 2 and 3 are located in the HAZ. As shown in Figure 5, the heating rates are much higher than the cooling rates. This is due to the following two reasons. One is that the isotherms in front of the heat source are compressed whereas those behind it are largely elongated due to the high welding speed. The other is that the existence of the volumetric heat source also contributes to the high heating rates. As expected, the peak temperatures are higher at locations close to the weld centre, and decrease as the monitoring location moves outwards. The calculated average cooling rate between 1 073 to 773 K (800 to 500 °C)
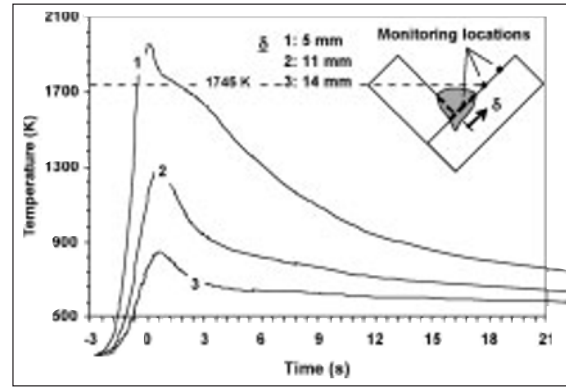
Symbol δ represents the distance from the joint root to a monitoring location at the top surface, as shown in the small figure.
Time zero is arbitrarily set to be correspondent to X = 0 mm location

Figure 5 – Calculated thermal cycles in the fillet weld

varies from 50 to 15 K/s for various welding conditions shown in Table 1. Furthermore, the average cooling rate decreases as the heat input per unit length increases. The value of the calculated cooling rate and its dependence on the welding parameters are consistent with those estimated using the nomograph available in the literature [33].

3.2 Estimation of unknown parameters using inverse modelling

The evolution of weld pool involves complex interaction of physical processes such as application of welding arc, metal droplet transfer, heat transfer through conduction and convection, free surface deformation and the fluid flow inside the weld pool. To simulate these simultaneous processes in the numerical heat transfer and fluid flow analysis, several input parameters are needed amongst which the values of η, k_{eff} and μ_{eff} are not known beforehand.

3.2.1 Effect of the effective thermal conductivity and viscosity on weld geometry

The effects of variation of effective thermal conductivity and effective viscosity on the weld geometry i.e. actual throat, penetration and leg length are presented in Figures 6 to 8 for case #1 in Table 1. Actual throat, penetration and leg length are non-dimensionalized by dividing the numerically obtained values with the corresponding experimental values. Figures 6 and 7 show that non-dimensional value of actual throat and penetration decrease with increase in the value of μ_{eff}. This is due to the fact that at higher values of μ_{eff}, the liquid metal velocities are low. As a result, the rate of convective heat transfer is diminished and the weld pool size is reduced. Figure 8 shows that the non-dimensional leg length decreases with increase in k_{eff}. The higher values of the effective thermal conductivity lower
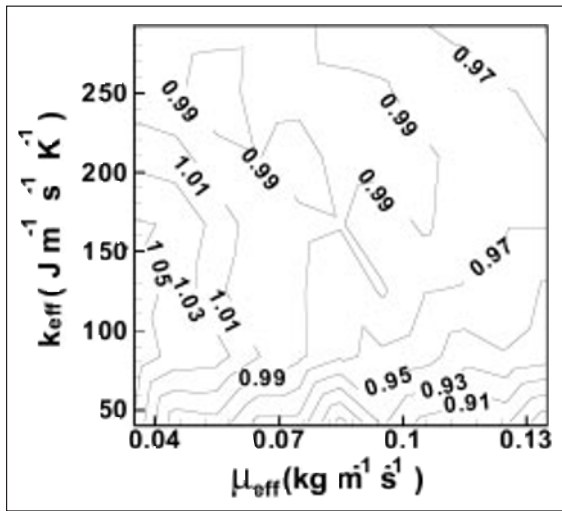
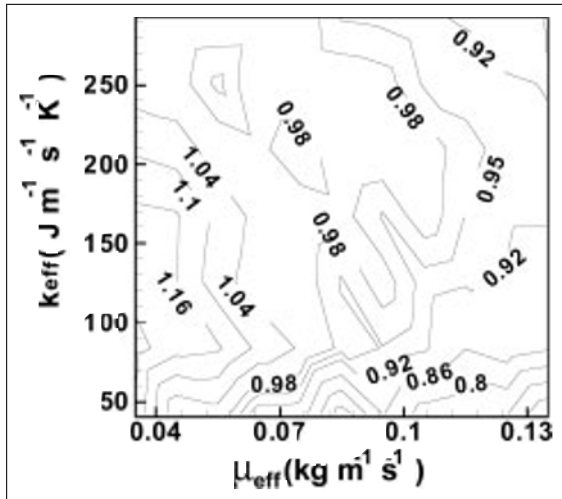**Figure 6 – Contour plot of the non-dimensional actual throat value for case #1 given in Table 1**

Figure 7 – Contour plot of the non-dimensional penetration value for case #1 given in Table 1
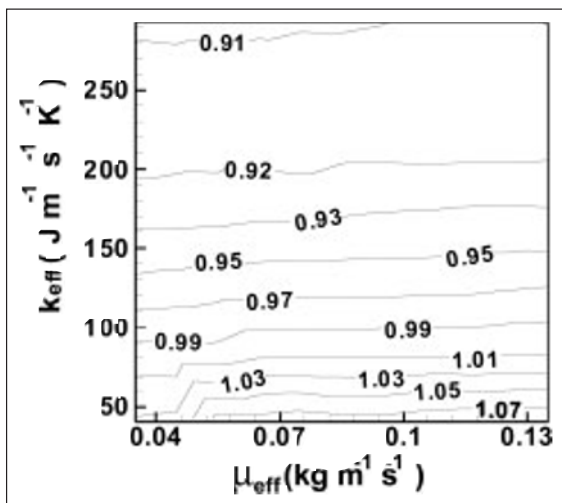

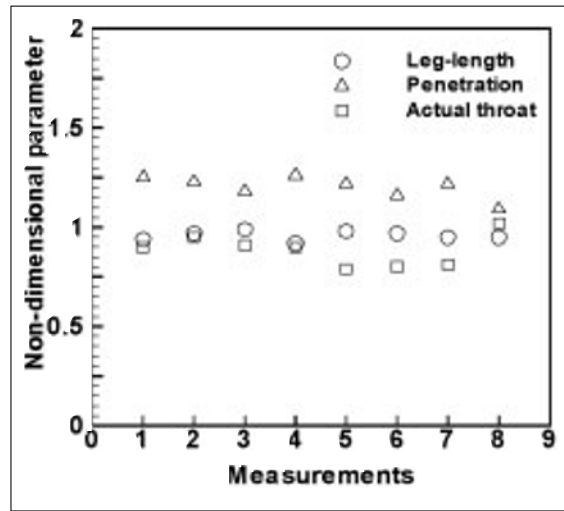**Figure 8 – Contour plot of the non-dimensional leg length value for case #1 in Table 1**

Figure 9 – Computed values of non-dimensional actual throat, penetration and leg length using $\eta = 0.59$, $k_{eff} = 209.0$ J m^{-1} s^{-1} K^{-1} and $\mu_{eff} = 0.12$ kg m^{-1} s^{-1} for all the eight measurement cases listed in Table 1

the resulting temperature gradient. The lower temperature gradient, in turn, decreases the convective heat transport and results in smaller leg length at high values of k_{eff}.

Figure 9 shows the non-dimensional penetration, actual throat and leg length obtained by using the values of arc efficiency as 0.54, $k_{eff} = 209.0$ J m^{-1} s^{-1} K^{-1} and $\mu_{eff} = 0.12$ kg m^{-1} s^{-1} as suggested in the literature [11, 13,14]. The non-dimensional penetration value obtained using these values are more than 1.0 for most of the cases. Therefore, the suggested combination of μ_{eff} and k_{eff} will not lead to optimum prediction of geometry for the weld conditions studied here and a set of optimised values of η, μ_{eff} and k_{eff} is needed.

3.2.2 Estimation of the unknown parameters

Table 3 shows the calculated values of these unknown parameters obtained by using different techniques. The progress in the optimisation of the two unknown parameters related to arc efficiency is shown in Figures 10 and 11. The values of these two parameters related to arc efficiency decrease slightly and finally reach almost same optimised values by different techniques. All the other unknown variables also show a similar trend and finally attain optimised values. Figure 12 depicts the variation in least square error (i.e. O(f)) with number of iterations. The objective function decays rapidly in the first 4 iterations in the LM method and both versions of CG. After that the objective function becomes almost constant for some iteration and then starts fluctuating. Table 3 shows that the Fletcher and Reeves's CG method gives somewhat better convergence of the objective function compared to other two methods. By using this method, the minimum value of the objective function obtained is 0.22 after 13 iterations while LM and Polak-Ribiere's CG method produced the value as 0.27 and 0.26 in 13 and 14 iterations, respectively.

Table 3 – Comparison of results obtained by using LM method and the two CG methods

Method	Parameters	Estimates	O(f)	Iterations	Probability
LM method	f_1	0.34	0.27	13	0.99
	f_2	6.00			
	f_3	2.10			
	f_4	1.99			
	f_5	2.79			
	f_6	2.82			
CG method- Fletcher and Reeves	f_1	0.31	0.22	13	0.99
	f_2	5.97			
	f_3	2.10			
	f_4	1.96			
	f_5	2.46			
	f_6	2.02			
CG method-Polak and Ribiere	f_1	0.34	0.26	14	0.99
	f_2	5.75			
	f_3	2.09			
	f_4	2.08			
	f_5	3.66			
	f_6	4.14			
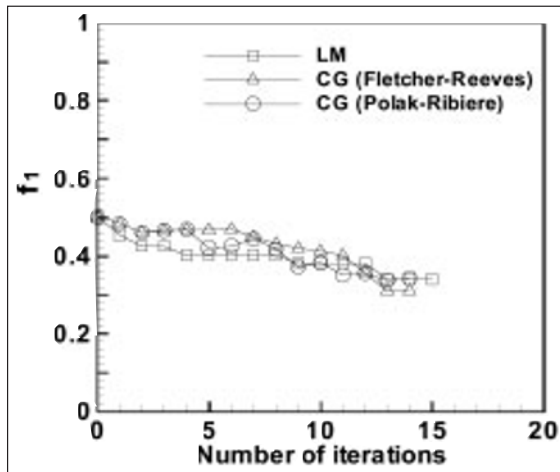
Figure 10 – Comparison of calculation progress of unknown variable f_1 using LM method and the two versions of CG method
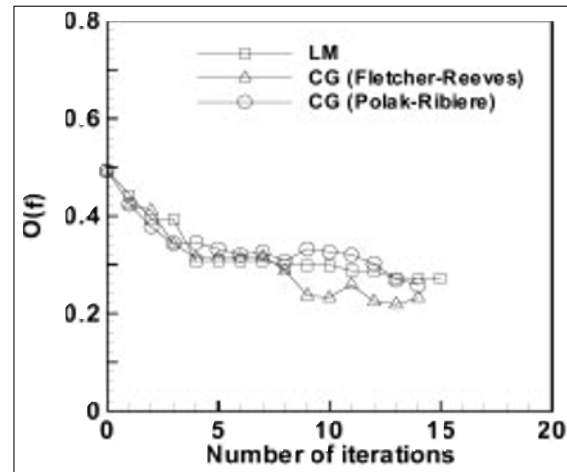

Figure 12 – Comparison of calculation progress of the objective function, O(f), using LM method and the two versions of CG method
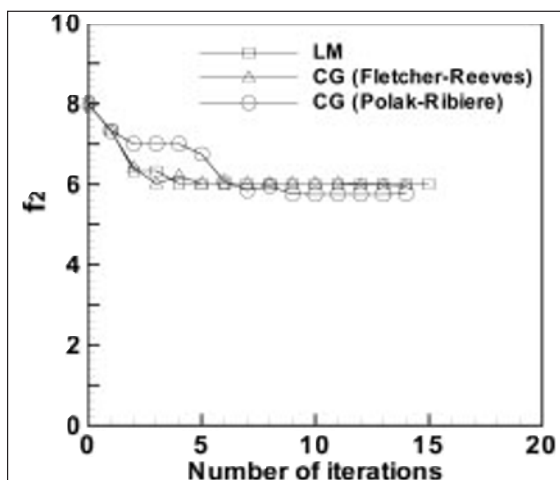

Figure 11 – Comparison of calculation progress of unknown variable f_2 using LM method and the two versions of CG method

3.2.3 Arc efficiency, effective thermal conductivity and viscosity

As the optimum combination of the unknown parameters are reached, the individual influence of a specific parameter on the dependent variables, contained in the sensitivity terms, may become very small or zero. The maximization of sensitivity matrix is generally aimed in order to estimate the optimum values [24-26, 32] of these unknown parameters. Figure 13 shows the variation of the determinant of the sensitivity matrix with iteration. The determinant of the sensitivity matrix does not significantly change with number of iterations after 12 iterations. The figure also shows that the values obtained by Fletcher-Reeves's CG method are the best optimal values because this method gives the highest value of the sensitivity matrix. The sensitivity coefficients and correlation coefficients of the matrix J^TJ are given in Tables 4 and 5. The correlations coefficients C_{ij} given in
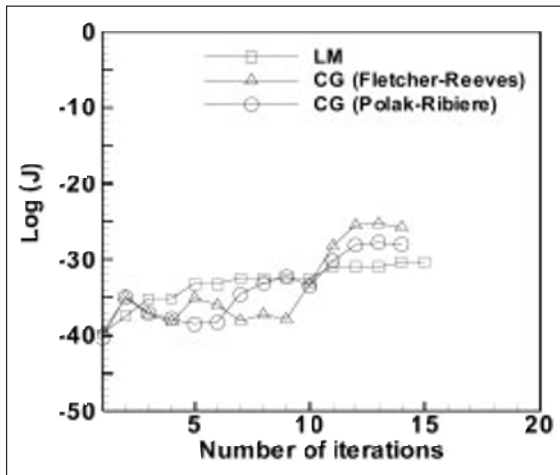
Figure 13 – Variation of the logarithmic of the determinant of the sensitivity matrix with number of iteration during all the three methods

Table 5 are computed from Table 4 using the following relation:

$$C_{ij} = \frac{A_{ij}}{\sqrt{A_{ii}\,A_{jj}}} \tag{46}$$

where

A_{ij} is the ij[th] component of the J^TJ matrix.

The correlations given in Table 5 indicate a large correlation between f_3, f_4, f_5 and f_6 while f_1 and f_2 has very low correlations with f_3, f_4, f_5 and f_6. It shows that values of effective thermal conductivity and effective viscosity depend significantly on the value of the efficiency. It also shows that the values of arc efficiency, effective thermal conductivity and effective viscosity are inter-dependent and varies with change in any value of these parameters.

A rational way to describe the optimum combination of the six unknown parameters is as a set of system prop-erties that is inherent within the eight measured weld samples governed by the optimisation calculation. Using the model, the optimal value of these unknown para-meters for the welding conditions listed in Table 1 can be expressed as:

$$\eta = 0.31 + 4.65 \times 10^{-6}\, \frac{IV}{w_f} \tag{47}$$

$$k_{eff} = 41.80 + 3.17 \times 10^{-5}\, \frac{IV}{U_w} \; (W/m - K) \tag{48}$$

$$\mu_{eff} = 0.016 + 1.05 \times 10^{-8}\, \frac{IV}{U_w} \; (kg/m - s) \tag{49}$$

where

I is the current (A),
V is voltage (V),
w_f is the wire feeding speed (m/s) and
U_w is the welding speed (m/s).

The values of η, k_{eff} and μ_{eff} are calculated by using equations (47), (48) and (49), for the experimental con-ditions given in Table 1. Table 6 shows that the effi-ciency increases slightly with the increase in input power and decrease in the wire feeding rate (case #3 and case #7 of Table 1). Table 6 also shows that there can be 50 % variation in the value of effective thermal conduc-tivity depending on the experimental conditions. The optimised values give enhancement factors of 5 and 7 for thermal conductivity and viscosity, respectively. Hong and Weckman [11, 13] suggested an enhancement fac-tor between 12 to 15 for thermal conductivity and a fac-tor more than 10 for the viscosity for 150 A current and 25 V power supply. Choo and Szekely suggested an enhancement factor of more than 8 times for the ther-mal conductivity and a factor of 30 for the viscosity for a current of 100 A. But the values available in the liter-ature [11, 13, 14] are independent of each other. There is no guidance available about the selection the values of these parameters for specific welding conditions.

The computed μ_{eff} and k_{eff} indicate that the rates of trans-port of momentum and heat are higher than that from laminar flow. The relation between the two variables is

Table 4 – Sensitivity matrix, J^TJ, obtained for the six unknown parameters estimated by using Fletcher-Reeves's CG method

Non-dimensional parameters	f_1	f_2	f_3	f_4	f_5	f_6
f_1	668.58	20.21	15.45	18.96	18.84	22.43
f_2	20.21	0.67	0.45	0.57	0.51	0.60
f_3	15.45	0.45	0.75	0.89	0.92	1.10
f_4	18.95	0.57	0.89	1.14	1.10	1.30
f_5	18.84	0.51	0.92	1.10	1.21	1.44
f_6	22.43	0.60	1.10	1.30	1.34	1.72

Table 5 – Correlation matrix obtained for the sensitivity coefficients in J^TJ from Table 4

Non-dimensional parameters	f_1	f_2	f_3	f_4	f_5	f_6
f_1	1					
f_2	0.95	1				
f_3	0.70	0.63	1			
f_4	0.69	0.65	0.96	1		
f_5	0.66	0.57	0.96	0.94	1	
f_6	0.66	0.56	0.97	0.93	0.93	1

Table 6 – Comparison of optimized values of arc efficiency, effective thermal conductivity and viscosity for eight test cases

	LM method			CG method- Fletcher and Reeves			CG method- Polak and Ribiere		
	η	k_{eff} (J/m-s-K)	μ_{eff} (kg/m-s)	η	k_{eff} (J/m-s-K)	μ_{eff} (kg/m-s)	η	k_{eff} (J/m-s-K)	μ_{eff} (kg/m-s)
1	0.61	112.87	0.05	0.58	112.86	0.04	0.60	121.22	0.07
2	0.59	96.15	0.04	0.56	96.14	0.03	0.58	100.32	0.06
3	0.62	91.97	0.04	0.59	91.96	0.03	0.61	96.14	0.06
4	0.60	133.77	0.05	0.57	133.76	0.04	0.59	137.94	0.08
5	0.58	87.79	0.04	0.55	87.78	0.03	0.57	87.78	0.05
6	0.60	112.87	0.05	0.57	112.86	0.04	0.59	117.04	0.08
7	0.57	121.22	0.05	0.54	121.22	0.04	0.56	125.4	0.08
8	0.58	96.15	0.04	0.55	96.14	0.03	0.57	100.32	0.06

governed by the turbulent Prandtl number (Pr), which is defined as:

$$Pr = \frac{\mu_T C_{PL}}{k_T} \qquad (50)$$

where

$\mu_{eff} = \mu_L + \mu_T$ and

$k_{eff} = k_L + k_T$;

μ_T and k_T are the artificial enhancement respectively in viscosity and conductivity to account for the fluctuating fluid movement and resulting enhanced transport of heat and mass within the weld pool.

The value of Pr available in the literature [13, 14] for a fully developed turbulent flow is 0.9, while Pr is below 0.1 for the laminar flow. The optimised combination of f_1, f_2, f_3, f_4, f_5 and f_6 obtained from LM method (in Table 3) results in Prandtl numbers between 0.35 to 0.40. The values of the Prandtl number lie between laminar and turbulent flow which suggests that the flow in GMAW fillet weld is not fully turbulent for the welding conditions given in Table 1.

3.2.4 Chi-Square Probability analysis

Chi-square probability, $P(\chi^2 | N)$, gives a quantitative measure for the goodness-of-fit of the model. It is defined as the probability that observed chi-square for a correct model should be less than a value χ^2.

The functions have the limiting values:

$$P(0|N) = 0 \text{ and } P(\infty|N) = 1 \qquad (51)$$

And the following relations to incomplete gamma functions:

$$P(\chi^2|N) = P(N / 2, \chi^2/2) \qquad (52)$$

Press *et al.* suggested [32] that if there exists a very high probability for some particular data set, then the apparent discrepancies are unlikely to be chance fluctuations. If value of chi-square probability is less than 0.999, then the fit may be acceptable if the errors in measurements are non-normal or have been moderately underestimated. If probability is larger than 0.999, then the estimation procedure or the model is doubtful. Based on the arguments given by Press *et al.* [32], we find that three models always give an acceptable value of probability i.e. 0.99 as shown in Table 3. It shows that obtained optimised values are acceptable for the experimental conditions given in Table 1.

Figure 14 depicts p_m^*, l_m^* and t_m^* as calculated using these optimised values of the unknown parameters. The welding process parameters and material properties such as welding current, voltage and weld speed corresponding to the measurements referred in Figure 14 are given in Tables 1 and 2, respectively. The non-dimensional values of actual throat and leg length obtained using these optimised parameters are much better than those obtained in Figure 9 for all the eight cases. Figure 15 shows a satisfactory agreement between the computed and the experimentally obtained weld geometry. The calculated geometric features of the fillet weld could be satisfactorily predicted by the using the optimised values of parameters in the numerical heat transfer and fluid flow model.

4 SUMMARY AND CONCLUSIONS

A smart phenomenological model for GMA fillet welding involving numerical calculation of heat transfer and fluid flow and parameter optimisation was developed. The
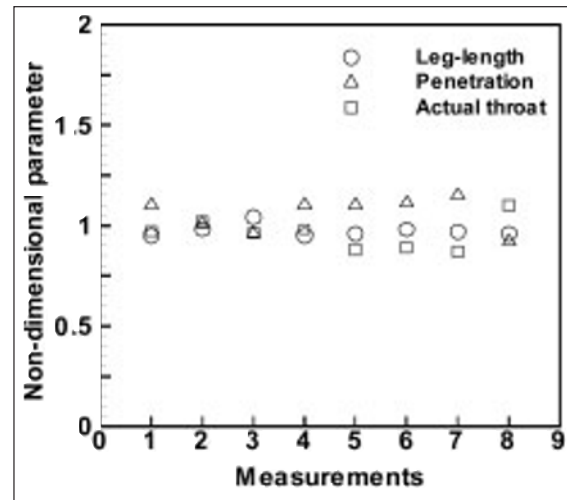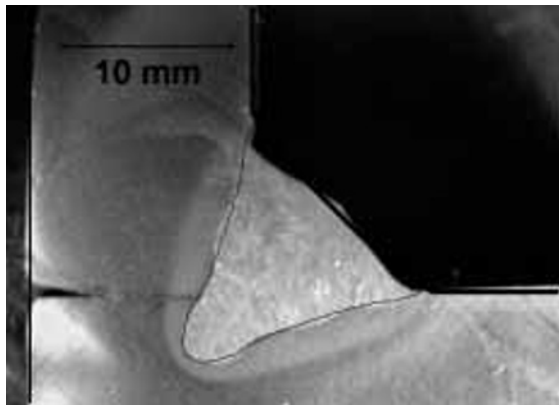

Figure 14 – Computed values of non-dimensional actual throat, penetration and leg length using the optimised set of six unknown parameters for all the eight measurement cases listed in Table 1

The solid line represents the calculated fusion zone boundary.

Figure 15 – Comparison between the calculated and experimental weld geometry for case #2 given in Table 1

model solved continuity, momentum and energy conservation equations in a curvilinear coordinate to obtain the temperature and velocity fields and surface profile during GMA fillet welding. Several optimisation methods for parameter estimation were considered including the Levenberg-Marquardt method, Fletcher-Reeve and Polak-Ribiere's modified conjugate gradient methods. The smart model was used to estimate the arc efficiency, effective thermal conductivity and viscosity variation as a function of welding conditions. The following conclusions can be drawn from this study.

(1) The heat transfer and fluid flow calculation indicated that in the weld pool, the liquid metal was driven mainly by the electromagnetic force and the Marangoni shear stress and, to a much lesser extent, by the buoyancy force. The liquid metal convection played a dominant role in dissipating the heat in the pool. The convection determined the temperature distribution and shape of the weld pool.

(2) This model could estimate the unknown parameters such as arc efficiency, effective thermal conductivity and effective viscosity based on only a few experimental measurements. The optimisation scheme required extensive sensitivity analysis of these unknown parameters based on the heat input, welding speed and wire feeding rate on the weld geometry. It is concluded that the enhancement in arc efficiency, effective thermal conductivity and effective viscosity should be a function of welding conditions instead of a single value. Fletcher-Reeves's conjugate gradient method gave the fastest convergence. The accuracy of the estimated set of the unknown parameters was verified using the numerical heat transfer and fluid flow model and the experimental data.

The values of the parameters determined in this investigation are useful for numerical heat transfer and fluid flow calculations. Furthermore, the smart phenomenological modelling and its application described in this paper is a contribution to the growing quantitative knowledge base in fusion welding.

REFERENCES

[1] Kim C.H., Zhang W., DebRoy T.: Modelling of temperature field and solidified surface profile during gas metal arc fillet welding, J. Appl. Phys., 2003, 94, pp. 2667-2679.

[2] Zhao H., DebRoy T.: Macro-porosity free aluminium alloy weldments through numerical simulation of keyhole mode laser welding, J. Appl. Phys., 2003, 93, pp. 10089-10096.

[3] Zhang W., Roy G., Elmer J.W., DebRoy T.: Modelling of heat transfer and fluid flow during gas tungsten arc spot welding of low carbon steel, J. Appl. Phys., 2003, 93, pp. 3022-3033.

[4] He X., Fuerschbach P.W., DebRoy T.: Heat transfer and fluid flow during laser spot welding of 304 stainless steel, J. Phys. D: Appl. Phys., 2003, 36, pp. 1388-1398.

[5] Kumar A., DebRoy T.: Calculation of three-dimensional electromagnetic force field during arc welding, J. Appl. Phys., 2003, 94, pp. 1267-1277.

[6] Elmer J.W., Palmer T.A., Zhang W., Wood B., DebRoy T.: Kinetic modelling of phase transformations occurring in the HAZ of C-Mn steel welds based on direct observations, Acta Mat., 2003, 51, pp. 3333-3349.

[7] Zhang W., Elmer J.W., DebRoy T.: Modelling and real time mapping of phases during GTA welding of 1005 steel, Mat. Sci. Eng. A, 2002, 333, pp. 321-335.

[8] Hong T., DebRoy T.: Effects of time, temperature and steel composition on the growth and dissolution of inclusions in liquid steels, Ironmaking and Steelmaking, 2001, 28, pp. 450- 454.

[9] Yang Z., Sista S., Elmer J.W., DebRoy T.: Three Dimensional Monte Carlo Simulation of Grain Growth during GTA Welding of Titanium, Acta Mat., 2000, 48, pp. 4813-4825.

[10] Yang Z., Elmer J.W., Wang J., DebRoy T.: Evolution of titanium arc weldment macro- and microstructures – Modelling and real time mapping of phases, Weld. J., 2000, 79, pp. 97-112.

[11] Hong K., Weckmann D.C., Strong A.B., Zheng W.: Modelling turbulent thermofluid flow in stationary gas tungsten arc weld pools, Sci. Technol. Weld. Joining, 2002, 7, pp. 125-136.

[12] Jonsson P.G., Szekely J., Choo R.T.C., Quinn T.P.: Mathematical models of transport phenomena associated with arc welding process: a survey, Model. Simul. Mater. Sci. Eng., 1994, 2, pp. 995-1016.

[13] Hong K., Weckman D.C., Strong A.B., Pardo E.: Proceedings of the First Int. Conference on Transport Phenomena in Processing, Hawaii, ed. by Secuk I. Guceri, Technomic Pub., 1992, pp. 626- 635.

[14] Choo R.T.C., Szekely J.: The possible role of turbulence in GTA weld pool behaviour, Weld. J., 1994, 73, pp. 25-31.

[15] De A., DebRoy T.: Probing unknown welding parameters from convective heat transfer calculation and multivariable optimisation, J. Phys. D: Appl. Phys., 2004, 37, pp. 140-150.

[16] Zhang W., Kim C.H., DebRoy T.: Heat transfer, fluid flow and solidified surface profile during gas metal arc fillet welding, unpublished document, Department of Materials Science and Engineering, The Pennsylvania State University, August 2003.

[17] S. Kou Y.H. Wang: Weld pool convection and its effect, Metallurgical Transactions B, 1986, 17, pp. 2271-2278.

[18] Voller V.R., Prakash C.: A fixed grid numerical modelling methodology for convection-diffusion mushy region phase-change problems, Int. J. Heat Mass Transfer, 1987, 30, pp. 1709-1719.

[19] Hoffmann K.A., Chiang S.T.: Computational fluid dynamics for engineering – Volume II, Engineering Education System, Wichita, KS, USA, 1993.

[20] Thompson J.F., Warsi Z.U.A., Wayne Mastin C.: Numerical grid generation: fundamentals and applications, Elsevier Science, New York, 1985.

[21] Patankar S.V., Numerical heat transfer and fluid flow, McGraw-Hill, New York, 1982.

[22] Lin M.L., Eagar T.W.: Pressures produced by gas tungsten arcs, Metall. Trans. B, 1986, 17B, pp. 601-607.

[23] Beck J.V.: Modelling of casting, welding and advanced solidification process V, ed. by M. Rappaz, M.R. Orzu, and K.W. Mahin, The Minerals, Metals & Materials Society, Warrendale, PA, 1991, pp. 503-518.

[24] Beck J.V., Blackwell B. C.R. St. Clair: Inverse heat conduction: Ill-Posed Problems Wiley International, NY, 1985.

[25] Beck J.V., Arnold K.J.: Parameter estimation in engineering and science, John Wiley and Sons, NY, 1977.

[26] Ozisik M.N., Orlande H.R B.: Inverse heat transfer: Fundamentals and applications, Taylor and Francis, NY, 2000.

[27] Bard Y.: Nonlinear parameter estimation, Academic Press, NY, 1974.

[28] Dennis J., Schnabel R.: Numerical methods for unconstrained optimisations and non-linear equations, Prentice Hall, 1983.

[29] Tikhonov N.: Solution of incorrectly formulated problems and the regularization method, Soviet Math. Dokl., 1963, 4, pp. 1035-1038.

[30] Fletcher R., Reeves C.M.: Function minimization by conjugate gradients, Computer J., 1964, 7, pp. 149-154.

[31] Tikhonov N.: Regularization of incorrectly posed problems, Soviet Math. Dokl., 1963, 4, pp. 1624-1627.

[32] Alifanov M.: Inverse heat transfer problems, Springer-Verlag, NY, 1994.

[33] Masubuchi K.: Analysis of welded structures, Pergamon, Oxford, 1980.